

Comparison of 3D structured illumination microscopy configurations in terms of spectral signal to noise ratio

Brudanin, Valerii; Rieger, Bernd; Stallinga, Sjoerd

DOI

[10.1364/OE.553750](https://doi.org/10.1364/OE.553750)

Publication date

2025

Document Version

Final published version

Published in

Optics Express

Citation (APA)

Brudanin, V., Rieger, B., & Stallinga, S. (2025). Comparison of 3D structured illumination microscopy configurations in terms of spectral signal to noise ratio. *Optics Express*, 33(5), 11832-11852. <https://doi.org/10.1364/OE.553750>

Important note

To cite this publication, please use the final published version (if applicable). Please check the document version above.

Copyright

Other than for strictly personal use, it is not permitted to download, forward or distribute the text or part of it, without the consent of the author(s) and/or copyright holder(s), unless the work is under an open content license such as Creative Commons.

Takedown policy

Please contact us and provide details if you believe this document breaches copyrights. We will remove access to the work immediately and investigate your claim.



Comparison of 3D structured illumination microscopy configurations in terms of spectral signal to noise ratio

VALERII BRUDANIN, BERND RIEGER,  AND SJOERD STALLINGA* 

Department of Imaging Physics, Delft University of Technology, The Netherlands

**s.stallinga@tudelft.nl*

Abstract: Structured illumination microscopy (SIM) is a powerful method for high-resolution 3D-imaging that is compatible with standard fluorescence labeling techniques, as it provides optical sectioning as well as an up to twofold improvement of lateral resolution over widefield microscopy by combining illumination pattern diversity with computational reconstruction. We present a quantitative analysis of the image quality of 3D-SIM using the spectral signal-to-noise ratio (SSNR). In particular, we compare conventional woodpile illumination pattern based 3D-SIM, where the pattern is rotated and translated to acquire the set of raw images that is fed into the reconstruction algorithm, to (square or hexagonal) lattice 3D-SIM, where the pattern is only translated to assemble the input set of raw images. It appears that conventional 3D-SIM has better SSNR than the considered cases of lattice 3D-SIM. In addition, we have also analyzed the impact of the relative amplitude, angle of incidence and polarization of the set of illumination plane waves on image quality, and show how two SSNR derived metrics, SSNR volume and SSNR entropy, can be used to optimize these illumination pattern parameters.

Published by Optica Publishing Group under the terms of the [Creative Commons Attribution 4.0 License](https://creativecommons.org/licenses/by/4.0/). Further distribution of this work must maintain attribution to the author(s) and the published article's title, journal citation, and DOI.

1. Introduction

Structured illumination microscopy [1–3] has attracted a lot of attention from the life sciences community since its appearance at the end of the previous century. SIM is a super-resolution and optical sectioning technique that enables large field-of-view live-cell imaging that is compatible with all fluorophores. The general idea behind SIM is to bypass the diffraction limit by downshifting high spatial frequencies within the band limit (Moire effect). This is achieved by spatial modulation of the sample fluorescence, and can be implemented in many different ways. Any microscopy technique involving non-uniform illumination can be interpreted as a form of SIM. This list includes, among others, confocal laser scanning microscopy (CLSM) [4], image scanning microscopy (ISM) [5–7], rescan confocal microscopy (RCM) [8], as well as 4pi [9,10] and array illumination [11,12] techniques. What separates SIM from these techniques is that the non-uniform illumination of the sample is spatially periodic, and is generally made using the interference of a finite number of plane waves. We will also restrain our attention to epi-illumination, as 4pi setups are not commonly used because of their experimental complexity. Finally, we will consider only the linear SIM regime. The fluorophore response is directly proportional to the illumination power in this regime, which entails that the resolution is limited by a sum of excitation and emission wavevectors. Non-linear SIM makes a theoretically unlimited resolution gain possible [13], but it requires high illumination power, and it results in increased photobleaching and photodamage. Relatively low intensity non-linear SIM modalities were proposed in combination with other methods [14], but their complexity prevents widespread application.

There are important differences between 2D-SIM and 3D-SIM concerning the illumination pattern and the resolution increase that can theoretically be achieved. In the case of 2D-SIM, all the illumination beams have the same angle of incidence on the focal plane, resulting in no interference in the axial direction. As a result, 2D-SIM provides an up to twofold increase in the lateral, but not in the axial, resolution. It does not provide Optical Sectioning (OS) because there is a so-called missing cone in the 3D spatial frequency space. The historically first version of SIM, however, did achieve OS using a smaller spatial frequency of the illumination pattern modulation in combination with a quadrature based real space reconstruction, but did not give any lateral resolution improvements [5,15]. This scheme was later applied in the context of light sheet microscopy for improving OS [16]. Currently, the most powerful approach to achieve both a lateral resolution improvement and OS is 3D-SIM, where a spatial modulation of the illumination pattern in both the lateral and axial direction is used [17,18].

Conventional 3D-SIM illumination contains two obliquely incident plane waves and one normally incident plane wave, all sharing the same linear polarization orthogonal to the shared plane of incidence (s-polarization) so as to maximize the modulation depth of the illumination pattern [19]. Such an illumination configuration is straightforward to implement experimentally, but it gives rise to interference only in one direction in the lateral plane. The resulting interference pattern exhibits a woodpile structure in 3D, with lateral cross-sections showing a striped pattern in one lateral direction only. In order to achieve a sufficiently isotropic resolution gain, the sample must be illuminated with this woodpile pattern rotated axially over at least three different angles. This is an experimentally complicated and slow process and was first implemented mechanically [17]. For 2D-SIM significant improvements in pattern switching speed were achieved recently with fast fiber optics [20]. This technology, however, has not been extended to 3D-SIM until now, as methods for fast and robust rotation of the polarization of the central beam are yet to be developed.

An alternative to this state-of-the-art three-beam SIM is so-called lattice SIM [21–23]. It engages more than two obliquely incident illumination waves to create a 2D intensity modulation in the lateral plane. The standard SIM reconstruction procedure can be readily adjusted to this case, and tedious illumination pattern rotations are avoided, as only 2D lateral shifts are required. This enables a noticeable acceleration of image acquisition, making the technique more suitable for imaging fast processes in living cells. A reduction in phototoxicity has also been reported [22,23]. 2D Bravais lattices with quasi-isotropic resolution increase permit square and hexagonal illumination patterns [21], which has been implemented by a number of groups [22,24,25]. Fully 3D illumination permits, in principle, other Bravais lattices [26]. In practice, however, we are usually limited with epi-illumination, which excludes symmetry groups of regular polyhedrons.

Every linear SIM configuration provides up to a two-fold resolution improvement that is more or less isotropic depending on the illumination scheme. In terms of the optical transfer function (OTF) it can be said that the OTF support is extended twice in the lateral direction. For 3D-SIM it is also extended in the axial direction, as the missing cone of spatial frequencies is filled. The axial OTF extension is not that simple to describe, however, due to the toric shape of the native widefield 3D-OTF. The shape and size of the OTF support is a key quality measure of any form of SIM. However, in practice, the situation is complicated by the presence of noise. Several noise sources can be suppressed or eliminated by engineering efforts, but shot noise cannot be avoided. The number of photons detected by a camera pixel is discrete and obeys the Poisson probability distribution. Spatial frequencies where the power of the signal is comparable with the power of the noise do not add any information to the imaging, and reconstruction can even result in image artifacts then. A detailed analysis of how noise of the acquired images propagates to the final SIM reconstruction was done in [27]. It was shown that the final noise distribution depends on the reconstruction procedure and is, generally, not white (flat in spatial frequency space) but coloured (peaked in spatial frequency space). Furthermore, while the image contrast

can be improved with regularization and apodization filters, the SSNR is independent of these free-to-choose functions. The SSNR only depends on physical quantities, namely the native widefield OTF, the characteristics of the illumination pattern, the noise level of the set of acquired images, and the fluorescent object itself. The SSNR is non-zero in the same region in spatial frequency space as the effective OTF, but it also assesses how reliably a given spatial frequency can be resolved. Thus, it is the SSNR that defines the fundamentally achievable quality of the reconstructed super-resolution image.

Previously, image quality inspection tools, such as SIMcheck [28] and SQUIRREL [29], have been applied to test or monitor SIM imaging, but these tools do not relate the underlying image formation to the proposed quality test measures. Li et al [30] compared the image formation of several microscopy contrast modalities, but did not consider multi-dimensional lattice illumination or the dependence of signal-to-noise characteristics on spatial frequency. Ingerman et al [31] studied the the impact of noise on linear and non-linear SIM, but restricted their attention to the 2D case. The goal of this paper is to improve on these previous works by using the SSNR as a measure to compare state-of-the-art 3D-SIM to lattice 3D-SIM. Different configurations of the illumination pattern are analysed in terms of their SSNR performance and the effect of several experimental parameters (angle of incidence, polarization, and relative beam power of the illumination plane waves) is evaluated. Pertinent differences between 2D and 3D-SIM that play a role in our extension of [31] are the increased complexity and variety of possible 3D illumination patterns, the role polarization of the illumination plane waves, and possible trade-offs between axial and lateral SSNR performance.

2. Theoretical background

We will assume that we can create in the back focal plane (BFP) of the objective lens a desired configuration of incoming plane waves, leading to a finite set of peaks in the Fourier space of intensity distribution in the excited volume. The complex amplitude of the electric field in the sample is:

$$\vec{E}(\vec{r}) = \sum_{i=1}^M \vec{A}_i \exp\left(2\pi i \vec{k}_i \cdot \vec{r}\right), \quad (1)$$

where M is the total number of plane waves, \vec{A}_i represents the amplitude and polarization vector of a plane wave component with a spatial frequency vector \vec{k}_i . The resulting intensity is:

$$\begin{aligned} h(\vec{r}) &= \left| \vec{E}(\vec{r}) \right|^2 \\ &= \sum_{l \in (x,y,z)} \sum_{i,j=1}^M \operatorname{Re} \left\{ A_{il} A_{jl}^* \exp\left(2\pi i (\vec{k}_i - \vec{k}_j) \cdot \vec{r}\right) \right\} \\ &= \sum_{\underline{mp}} a_{\underline{mp}} \exp\left(2\pi i \vec{k}_{\underline{mp}} \cdot \vec{r}\right). \end{aligned} \quad (2)$$

Here, the $a_{\underline{mp}}$ are the coefficients of the Fourier peaks of the intensity pattern, and the set $\vec{k}_{\underline{mp}}$ is the set of distinct spatial frequency vector differences $\vec{k}_i - \vec{k}_j$, and can be split into lateral (xy) and axial (z) parts by:

$$\vec{k}_{\underline{mp}} = \vec{k}_{\underline{m}} + k_{ax,p} \vec{e}_z, \quad (3)$$

where the spatial frequency vectors are labeled by the lateral indices $\underline{m} = (m_1, m_2)$:

$$\vec{k}_{\underline{m}} = m_1 \vec{b}_1 + m_2 \vec{b}_2. \quad (4)$$

Here basis vectors \vec{b}_1 and \vec{b}_2 span a Bravais lattice in the lateral (xy) part of reciprocal space. For state-of-the-art 3D-SIM one of the components is always zero ($m_2 = 0$), for lattice 3D-SIM both

components can be non-zero. The Fourier transform of the illumination pattern is the sum of delta-peaks:

$$\hat{h}(\vec{k}) = F[h(\vec{r})] = \sum_{mp} a_{mp} \delta(\vec{k} - \vec{k}_{mp}). \quad (5)$$

where $F[\cdot]$ stands for the Fourier transform.

The basic illumination pattern is translated and rotated to:

$$h_{rm}(\vec{r}) = h(R(\alpha_r, \vec{e}_z)(\vec{r} - \vec{u}_n)), \quad (6)$$

where $R(\alpha_r, \vec{e}_z)$ is the rotation matrix for a rotation over an angle α_r around the z axis \vec{e}_z , and where \vec{u}_n is a set of lateral (xy) translations. The index $r = 1, 2, \dots, M_r$, where M_r is the total number of rotations. For state-of-the-art 3D-SIM typically $M_r = 3$ or $M_r = 5$, for lattice SIM $M_r = 1$. The lateral translations are:

$$\vec{u}_n = u_{n1} \vec{a}_1 + u_{n2} \vec{a}_2, \quad (7)$$

where \vec{a}_1 and \vec{a}_2 span the lateral (xy) Bravais lattice in real space, and which satisfy:

$$\vec{a}_i \cdot \vec{b}_j = \delta_{ij}. \quad (8)$$

The translation components u_{n1} and u_{n2} are chosen to satisfy:

$$\sum_{n=1}^{M_t} \exp\left(2\pi i (\vec{k}_{\underline{m}} - \vec{k}_{\underline{m}'}) \vec{u}_n\right) = M_t \delta_{\underline{m}, \underline{m}'} = M_t \delta_{m_1 m_1'} \delta_{m_2 m_2'}. \quad (9)$$

where M_t is the total number of illumination pattern translations. For state-of-the-art 3D-SIM the translations are always one-dimensional ($n_2 = 0$), for lattice 3D-SIM both components are generally non-zero.

In this work we assume freely rotating emitters and that our imaging system satisfies Abbe's sine condition. The expression for the point spread function (PSF) in scalar imaging theory with high numerical aperture is provided in Ref. [32] and reads:

$$g(v, u) = C \left| \int_0^{\alpha_{so}} P(\alpha) \exp\left(\frac{i u}{2} \frac{\sin^2(\alpha/2)}{\sin^2(\alpha_{so}/2)}\right) J_0\left(v \frac{\sin(\alpha)}{\sin(\alpha_{so})}\right) \sin(\alpha) d\alpha \right|^2, \quad (10)$$

defined in terms of the corresponding dimensionless coordinates:

$$\begin{aligned} v &= \frac{2\pi}{\lambda} r NA, \\ u &= \frac{4\pi}{\lambda} z \left[n_s - \sqrt{n_s^2 - NA^2} \right], \end{aligned} \quad (11)$$

Here n_s is the refractive index in object space, which is assumed to be constant, NA is the numerical aperture of the system, $NA = n_m \sin(\alpha_{so})$, where n_m is a refraction index of immersion liquid, and α_{so} is the semi-opening angle of the objective lens. The function $J_0(\cdot)$ is the zeroth order Bessel function, and $P(\alpha) = \sqrt{\cos(\alpha)}$ is the apodization function according to the sine condition. The constant prefactor C is found from the condition that the sum of the PSF over all N camera pixels is unity.

This normalization ensures energy conservation in the sampled space. We do not expect any conclusions of this work to change substantially if a more elaborate vectorial PSF model [33] is used instead.

Throughout this work the following parameters are used $n_s = n_m = 1.5$, so we do not consider effects of refractive index mismatch. The semi-opening angle of the lens was chosen to be

72°, leading to $NA \approx 1.43$. This choice of parameters hardly affect the results on SSNR if the dependence of SSNR on spatial frequencies is given in units of the corresponding cut-off frequencies of a widefield microscope, i. e. correctly rescaled.

In our analysis we follow a discrete image formation model, where the set of pixel positions in real space \vec{r}_k can be labeled with an integer index $k = 1, 2, \dots, N$, with N the number of pixels of the camera, and where the set of pixel positions in Fourier space, i.e. the set of spatial frequency vectors \vec{q}_j , is labeled with an integer index $j = 1, 2, \dots, N$. The spectral signal to noise ratio depends on the index j of the spatial frequency vector \vec{q}_j by [27]:

$$SSNR(\vec{q}_j) = \frac{\hat{S}(\vec{q}_j)}{\hat{N}(\vec{q}_j)} = \frac{|\hat{D}(\vec{q}_j)|^2 |\hat{f}(\vec{q}_j)|^2}{\hat{V}(\vec{q}_j) \hat{f}_0 + N\sigma^2 \hat{D}(\vec{q}_j)}, \quad (12)$$

with \hat{S}_j and \hat{N}_j corresponding to spectral signal and noise power respectively. Here σ^2 denotes the variance of the readout noise and $\hat{f}(\vec{q}_j)$ is the Fourier transform (FT) of the object intensity, where \hat{f}_0 is a shorthand for the FT at spatial frequency zero. The functions $\hat{D}(\vec{q}_j)$ and $\hat{V}(\vec{q}_j)$ depend only on the physical parameters of the system, namely the illumination pattern parameters and the OTF of the microscope. Generalized expressions, valid for both state-of-the-art 3D-SIM and for lattice 3D-SIM, for the case where the illumination pattern is held fixed relative to the image plane are:

$$\hat{D}(\vec{q}_j) = M_t \sum_{\underline{m}} \sum_r |\hat{g}^{(\underline{m})}(\vec{q}_j - \vec{k}_{r\underline{m}})|^2 \quad (13)$$

$$\hat{V}(\vec{q}_j) = M_t \sum_{\underline{m}, \underline{m}'} \sum_r \hat{g}^{(\underline{m})}(\vec{q}_j - \vec{k}_{r\underline{m}}) \hat{g}^{(\underline{m}')}(\vec{q}_j - \vec{k}_{r\underline{m}'}) \hat{g}^{(\underline{m}-\underline{m}')}(\vec{k}_{r\underline{m}} - \vec{k}_{r\underline{m}'}). \quad (14)$$

Here the rotated spatial frequency vectors are:

$$\vec{k}_{r\underline{m}} = R(-\alpha_r, \vec{e}_z) \vec{k}_{\underline{m}} \quad (15)$$

and the effective optical transfer functions $\hat{g}^{(\underline{m})}$ are the linear combinations:

$$\hat{g}^{(\underline{m})}(\vec{q}_j) = \sum_p a_{\underline{m}p} \hat{g}(\vec{q}_j - k_{ax,p} \vec{e}_z). \quad (16)$$

Eq. (16) expresses the fact that we do not separate all Fourier components in the reconstruction procedure. In case of state-of-the-art 3D-SIM, $\hat{g}^{(\underline{m})}(\vec{q})$ is equal to the 3D-OTF $\hat{g}(\vec{q})$ of the optical system when \underline{m} corresponds to in-plane Fourier harmonics (i.e. with $k^z = 0$) and to $(\hat{g}(\vec{q} + k_z \vec{e}_z) + \hat{g}(\vec{q} - k_z \vec{e}_z))/2$ otherwise.

The concept of SSNR is closely related to the concept of Fourier ring correlation (FRC) [34], which compares the consistency of two randomly split data halves across rings in spatial frequency space. FRC is most often used for assessing resolution limits by finding the spatial frequency where the FRC crosses a suitably chosen threshold. SSNR on the other other hand gives a full picture of imaging performance across all spatial frequencies. On average, the two quantities are related by [35]:

$$FRC \approx \frac{\langle SSNR \rangle}{1 + \langle SSNR \rangle}, \quad (17)$$

where the brackets indicate averaging over rings in spatial frequency space.

We will assume we are working in the shot noise dominated limit, which is realistic for modern cameras, i.e., $N\sigma^2 \hat{D}(\vec{q}_j) \ll \hat{V}(\vec{q}_j) \hat{f}_0$. Then we can separate in the expression for the SSNR the

physical imaging system dependent part from the object dependent part:

$$SSNR(\vec{q}_j) = \frac{|\hat{D}(\vec{q}_j)|^2}{\hat{V}(\vec{q}_j)} \times \frac{|\hat{f}(\vec{q}_j)|^2}{\hat{f}(\vec{0})} \equiv SSNR(\vec{q}_j)^I \times SSNR(\vec{q}_j)^O. \quad (18)$$

In the rest of this work we will focus on the imaging system dependent part $SSNR^I$, which we call the SSNR transfer function. While the actual SSNR eventually depends on the manifestation of given spatial frequencies in the object, the illumination dose, fluorescence strength, and overall photon detection efficiency, it is the SSNR transfer function $SSNR^I$ that suitable for a comparison between the performance of different 3D-SIM systems.

The difference between the functions $\hat{D}(\vec{q}_j)$ and $\hat{V}(\vec{q}_j)$ depends very much on the degree of overlap between the different OTF copies. In case the Fourier order overlap in the function $\hat{V}(\vec{q}_j)$ can be ignored, i.e. if:

$$g^{(m-m')}(\vec{k}_{r\bar{m}} - \vec{k}_{r\bar{m}'}) \approx a_0 \delta_{\underline{m}, \underline{m}'} \quad (19)$$

we find $\hat{V}(\vec{q}_j) \approx a_0 \hat{D}(\vec{q}_j)$, and $SSNR(\vec{q}_j)^I \approx \hat{D}(\vec{q}_j)/a_0$, where a_0 is the DC Fourier coefficient of the illumination pattern. When the illumination pattern is normalized such that the sum over all rotations and translations is equal to one we have $a_0 = 1/(M_t M_r)$. In this limit the general theory of [27] reduces to the theory of [31]. It is expected that the degree of Fourier order overlap is relatively high for e.g. spot array based 2D-SIM, where many Fourier orders participate, and moderate for small pitch line pattern based 2D-SIM, with a limited number of Fourier orders that are well separated in Fourier space. The degree of overlap is even smaller for state-of-the-art and lattice 3D-SIM, because the 3D-OTF has a more peaked shape than the 2D-OTF. In order to quantify this qualitative line of reasoning we computed the relative mean absolute difference:

$$RMAD = \frac{\sum_j |\hat{V}(\vec{q}_j)/a_0 - \hat{D}(\vec{q}_j)|}{\sum_j \hat{D}(\vec{q}_j)} \quad (20)$$

for three cases analyzed in Ref. [27], namely for DMD-based spot array scanning SIM [12], the Zeiss Elyra system used for single focal slice 2D-SIM [22] and the OMX Delta system used for 3D-SIM, and found values of 8.4%, 5.7%, and 2.3%, respectively, in agreement with the qualitative expectations.

The impact of a constant background b (in units photons/pixel) on the noise level is that it adds spatially uniform noise with standard deviation \sqrt{b} to all raw images. This is the same in overall appearance as Gaussian noise resulting from camera readout. The object DC component \hat{f}_0 appearing in the noise variance in Eq. (12) can be split into a foreground and background part, $\hat{f}_0 = \hat{f}_{0,s} + Nb$, and the relative importance of background for the SSNR thus follows the ratio between the average number of foreground photons per pixel $\hat{f}_{0,s}/N$ to the background per pixel b . The noise arising from the uniform background obviously decreases the SSNR, but it does not impact the imaging system dependent factor $SSNR^I$ we introduced in Eq. (18).

We will compare 3D-SIM configurations using two metrics based on the SSNR transfer function. The first is the SSNR volume:

$$SSNR_V = \sum_{j=1}^N SSNR(\vec{q}_j)^I. \quad (21)$$

In the limit in which we can ignore the Fourier order overlap this expression simplifies to:

$$\begin{aligned} \sum_j SSNR(\vec{q}_j) &\approx M_t M_r \sum_j \hat{D}(\vec{q}_j) \\ M_t^2 M_r \sum_r \sum_m \sum_j \left| \sum_p a_{mp} \hat{g}(\vec{q}_j - \vec{k}_{rm} - k_{ax,p} \vec{e}_z) \right|^2 & \\ \approx \hat{G}^2 \sum_{mp} \left| \frac{a_{mp}}{a_0} \right|^2 & \end{aligned} \quad (22)$$

where $\hat{G}^2 = \sum_j |\hat{g}(\vec{q}_j)|^2$, and where we ignored the axial order overlap as well, i.e. cross-terms $\hat{g}(\vec{q} - k_{ax,p} \vec{e}_z) \hat{g}(\vec{q} - k_{ax,p'} \vec{e}_z)$ for $p \neq p'$ are neglected.

The ratio a_{mp}/a_0 does not depend on the number of illumination pattern rotations and translations, implying that the SSNR volume also does not depend on M_r and M_t . The reason lies in the fact that eq. (13) and (14) apply to the same normalized illumination dose, meaning that an increase in the number of raw images per reconstructed super-resolved image means a smaller photon number per raw image. The SSNR volume depends only on the number and power of the Fourier peaks and not on their location in Fourier space. It is shown in this work, in particular, that the SSNR volume is insensitive to the angle of incidence of the plane waves on the sample if they are s-polarized. This means that SSNR volume is uncorrelated to the resolution gain in the limit where the Fourier orders do not overlap. The increase in the SSNR volume over the widefield case is equal to the total power of all Fourier peaks except for the zero order peak.

From the above it follows that the SSNR volume is insufficient for the evaluation of the potential resolution and isotropy of a given 3D-SIM configuration. One can come up with different measures for this purpose. We will consider a configuration to be better when it results in a more isotropic distribution of the SSNR in spatial frequency space. To that end we introduce the SSNR entropy:

$$SSNR_S^I = - \sum_{j=1}^N p_j \log(p_j), \quad (23)$$

with $p_j = SSNR(\vec{q}_j)^I / SSNR_V$, as a second system quality metric based on the SSNR transfer function.

The two chosen metrics $SSNR_V$ and $SSNR_S$ are always bigger for any SIM configuration than for the corresponding quantities in widefield microscopy. It is therefore convenient to consider their increase expressed in units of widefield SSNR volume and SSNR entropy respectively:

$$\begin{aligned} SSNR_V^{inc} &= \frac{SSNR_V^I - SSNR_{V,widefield}^I}{SSNR_{V,widefield}^I} \approx \sum_{mp} |a_{mp}|^2 - 1 \\ SSNR_S^{inc} &= \frac{SSNR_S^I - SSNR_{S,widefield}^I}{SSNR_{S,widefield}^I}. \end{aligned} \quad (24)$$

It can be seen that $SSNR_V^{inc}$ is independent of the microscope OTF. These quantities are positive everywhere and are less than one in all our simulations.

3. SIM configuration analysis

Using the formalism from the previous chapter, we analyze the performance of known SIM modalities. We compared widefield microscopy, state-of-the-art line pattern based 3D-SIM [17], square lattice 3D-SIM [21–23] and hexagonal lattice 3D-SIM [21,22]. Schematic illustrations

of BFP structures of the discussed SIM modalities are shown in Fig. 1. Animations of the corresponding 3-dimensional illumination patterns can be found in [Visualization 1](#) with a representative frame shown in Fig. 2. In the appendix we list the illumination electric fields for the different configurations, as well as the resulting non-zero Fourier peaks \vec{k}_{mp} and associated order strengths a_{mp} . To illustrate the effect of the polarization on the SSNR, two versions of square lattice SIM with five incident plane waves are considered. In the first case, the four obliquely incident plane waves are s-polarized, while the normally incident plane wave is linearly polarized at 45° with the planes of incidence of the obliquely incident plane waves. In the second case, all five plane waves share the same circular polarization. The use of uniform circular polarization may provide an advantage in experimental realization of lattice 3D-SIM. We also choose circular polarization for the normally incident plane wave in hexagonal SIM, as no linear polarization of a normally incident wave can provide equal interference with all the oblique ones in such cases.

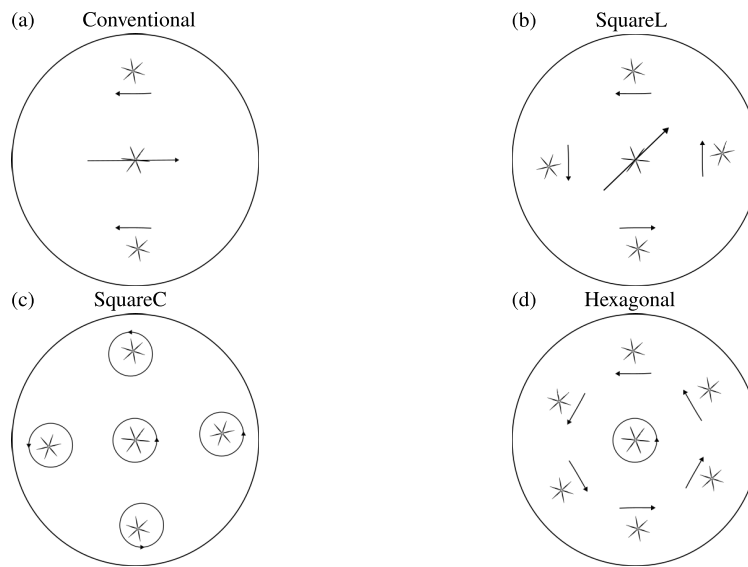


Fig. 1. Back focal plane illumination configurations for different 3D-SIM configurations. a) State-of-the-art 3D-SIM based on small pitch woodpile illumination pattern ("Conventional"). b) Square lattice 3D-SIM with linearly polarized plane waves ("SquareL"). c) Square lattice 3D-SIM with circularly polarized plane waves ("SquareC"). d) Hexagonal lattice SIM with linearly polarized plane waves ("Hexagonal").

To match experimental practice the angle of incidence of the obliquely incident plane waves θ_{inc} was chosen a bit less than a semi-opening angle of the lens α_{so} : $\sin \theta_{inc} / \sin \alpha_{so} = 0.9$, providing a resolution increase up to 1.9 the diffraction limits in the lateral directions (Stokes shift is ignored).

We define r as the ratio of field amplitudes of s -components of obliquely incident waves to the x or y component of the normally incident one. Then the power of Fourier peaks is proportional to r^2 for those belonging to the $q_x q_y$ -plane (lateral peaks) and to r for those that do not and are responsible for an axial resolution increase (axial peaks). The zeroth peak height is equal to the total power of illumination. Figure 3 shows $q_x q_y$ and $q_x q_z$ slices of the SSNR transfer function for particular values of the parameter r , the motivation for which is explained later. We consider natural units for spatial frequencies to be the cut-off frequencies of the widefield OTF. The lateral cut-off frequency (LCF) corresponds to $2NA/\lambda$, and the axial cut-off frequency (ACF) to $n_m(1 - \cos(\alpha_{so}))/\lambda$. The observed peaks correspond to the illumination structure, that should be

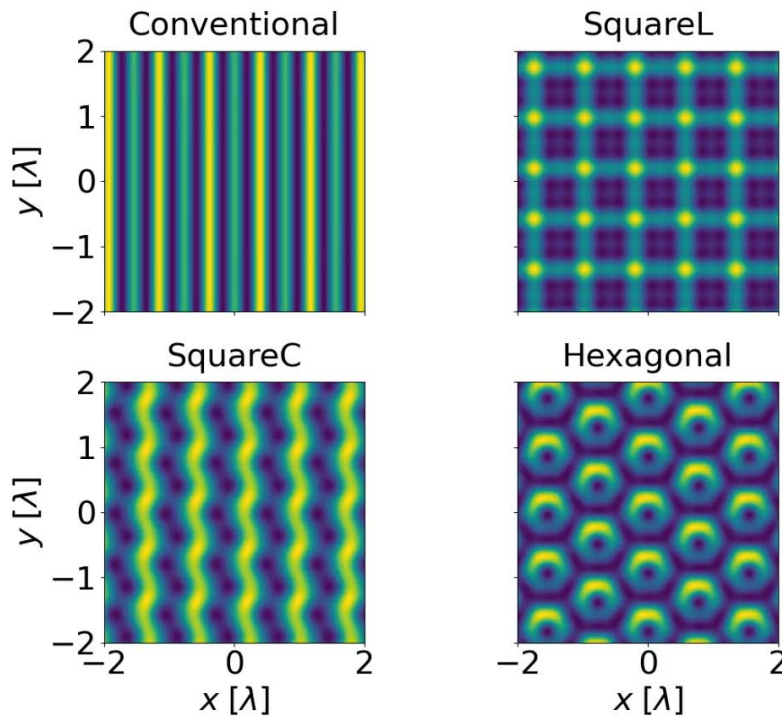


Fig. 2. Illumination structure of the configurations of interest in the slice $z = -\lambda$ (see Visualization 1).

understood as the rotational average of the illumination Fourier peaks if the number of rotations is higher than 1. In case of conventional SIM there are 6 lateral peaks - 2 per each rotation - and 12 axial ones (4 shown in the axial cross-section). Square lattice SIM with linearly polarized plane waves shows 4 lateral peaks and 8 axial peaks, while square lattice SIM with circularly polarized plane waves has 8 lateral peaks and 8 axial peaks. Hexagonal lattice SIM has 18 lateral peaks and 12 axial peaks. A large number of peaks ensures a higher homogeneity of the SSNR, but also requires a higher number of spatial shifts of the illumination pattern to disentangle the different image Fourier orders. This number is at least equal to the number of projections of the illumination peaks to the $q_x q_y$ plane, but may also be bigger when the orthogonality condition Eq. (9) is imposed. For example, hexagonal lattice SIM hence needs more raw images than conventional SIM.

Several observations can be made comparing square lattice illumination configurations with different polarization. The difference in polarization results in qualitatively different behaviour of the SSNR. In the case of linearly (s) polarized waves, no diagonal peaks are present in the Fourier domain. It means, in particular, that more raw images are required for the SIM reconstruction than in the case of circularly polarized waves. It is also clearly seen that square lattice SIM with circular polarization leads to a significant reduction of SSNR at high frequencies in comparison with linear polarization. As it is shown in the Appendix, for square illumination patterns, s-polarized waves give peaks with the magnitude r^2 independent on the angle of incidence, whereas for circularly polarized waves the amplitude of the same peaks changes to $r^4 \cos^4(\theta_{inc})$, which is considerably smaller for large θ_{inc} . The amplitude of the diagonal peaks in the latter case is $r^4 \sin^4(\theta_{inc})$, which grows with θ_{inc} , but which has a lateral position in Fourier space closer to the origin, i.e. it contributes to SSNR at smaller lateral spatial frequencies. Finally, an elliptically shaped anisotropy can be noticed in the case of circularly polarized waves. It appears that this

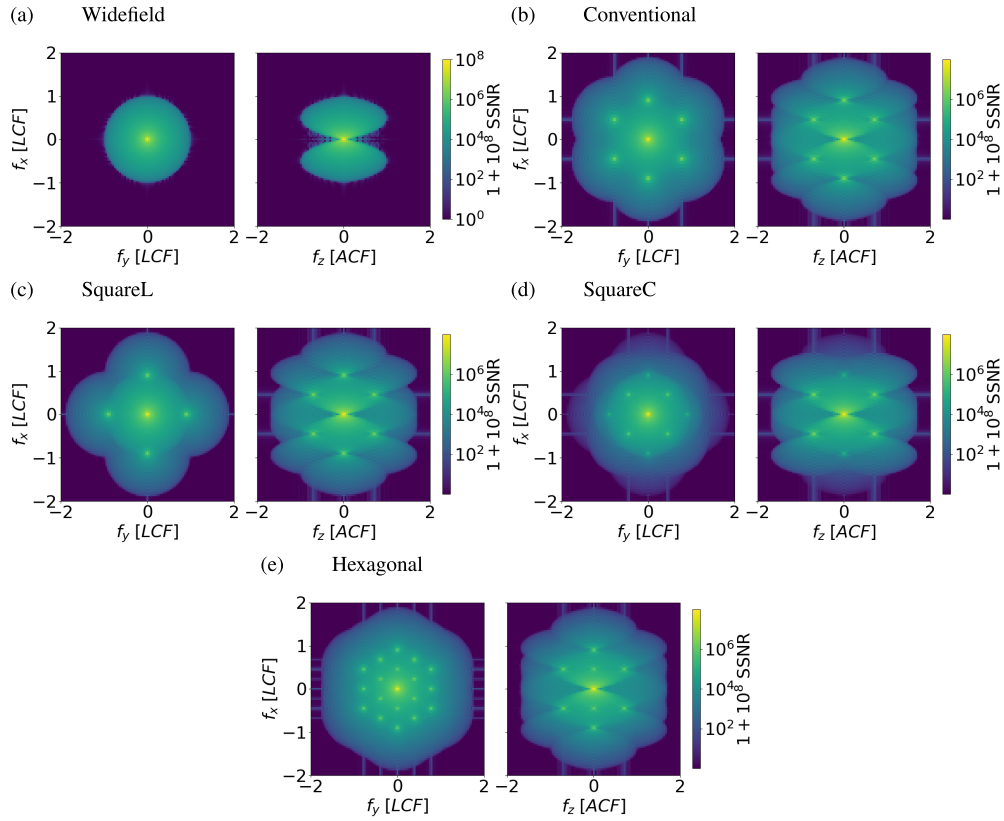


Fig. 3. Slices of the SSNR transfer function $SSNR^I$ along $q_z = 0$ and $q_y = 0$. a) Widefield. b) Conventional state-of-the-art SIM for $M_r = 3$ rotations and for $r = 1$. c) Square lattice SIM with linearly polarized incoming plane waves, for $r = 1$. d) Square lattice SIM with circularly polarized incoming plane waves, for $r = 0.55$. e) Hexagonal lattice SIM for $r = 1$.

effect is related to the choice of the mutual phases of the incoming plane waves, which we discuss in more detail below.

In Fig. 4, radial averages of the SSNR transfer function are shown for two planes. The plane $q_z = 0$ shows how configurations compare in terms of lateral SSNR and the plane $q_z = -ACF$ illustrates their axial performance, i.e., optical sectioning capabilities. Conventional SIM gives the highest peak at both axial and lateral cut-off frequencies, as well as the highest curve at super resolved frequencies above the LCF. An additional peak at the lower spatial frequency $LCF/\sqrt{2}$ is seen for circularly polarized square lattice SIM, and two more peaks at $\sqrt{3}LCF/2$ and $LCF/2$ are present for hexagonal lattice SIM, in correspondence to the observed Fourier structure. A poor performance of the configuration with circularly polarized waves in the lateral plane compared to the other configurations is apparent. It is also noted that the diagonal peaks hardly add any SSNR beyond the diffraction limit. Hexagonal lattice SIM shows high SSNR in the $q_z = 0$ plane, but shows the lowest radially averaged SSNR at $q_z = ACF$. The SSNR transfer function is more isotropic in this case than for other lattice SIM configurations, however, due to its intrinsic hexagonal symmetry.

The SSNR of all the configurations depends crucially on two parameters: r and θ_{inc} . We can employ global metrics $SSNR_V^I$ and $SSNR_S^I$ to investigate how their choice affects the SSNR. We can then derive the parameter values that give the best SSNR performance. The ratio r of

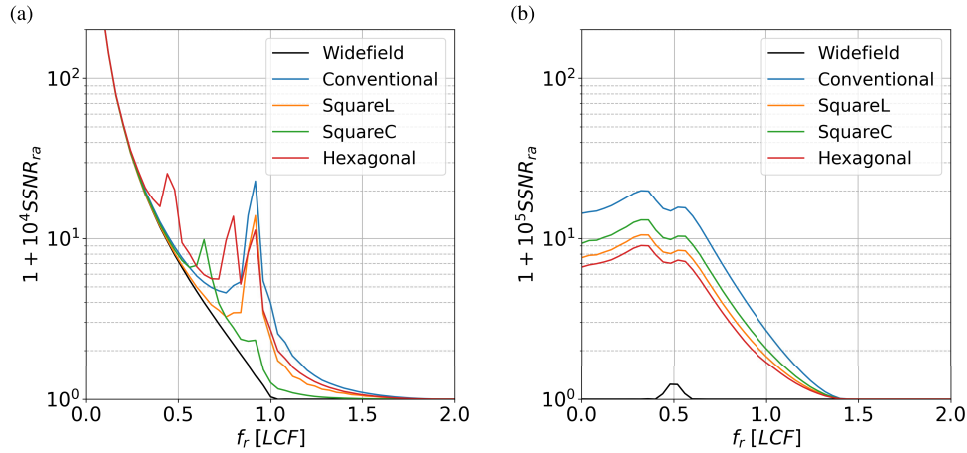


Fig. 4. Ring averaged SSNR transfer function. a) $q_z = 0$. b) $q_z = -1$ ACF

field strengths of obliquely incident and normally incident waves was found by maximizing Eq. (22). This maximization results in $r = 1$ for conventional SIM and square lattice SIM with s-polarized obliquely incident plane waves. For square lattice SIM with circularly polarized obliquely incident plane waves, the optimal ratio depends on the angle of incidence of incoming plane waves. It remains within the range of 0.5 – 0.6 for a broad range of angles, and is close to 0.58 for $\theta_{inc} \approx 58^\circ$ used in this work. The SSNR volume for hexagonal lattice SIM has its maximum at $r \rightarrow \infty$, which corresponds to the limiting case of 2D SIM, where there is no normally incident plane wave. This is due to the fact that the Fourier transform of the hexagonal illumination pattern has more lateral peaks than axial ones. The highest SSNR entropy is achieved for a finite value of r . It can be seen from the corresponding plot in Fig. 5 that to maximize SSNR entropy the value $r = 1$ must be chosen. At this value all the magnitudes of the SSNR peaks become the same for hexagonal lattice SIM. It turns out that the dependence of both SSNR_V^{inc} and SSNR_S^{inc} on r is qualitatively similar. This happens because the angle of incidence θ_{inc} is close to α_{so} . Then the increase in SSNR volume is mostly due to the high spatial frequencies, and these high spatial frequencies affect SSNR entropy the most.

We now analyze the effect of the angle of incidence of obliquely incident waves. The dependence of global metrics on θ_{inc} at the same α_{so} is plotted in Fig. 6. It appears that SSNR_S^{inc} grows monotonously with the angle of incidence. This is expected as more high spatial frequency content is observed at a smaller interference pitch. The line for square lattice SIM with circularly polarized obliquely incident plane waves has a smaller slope at big angles than for square lattice SIM with linearly polarized obliquely incident plane waves. This happens due to the decrease of height of the high spatial frequency lateral peaks as $\cos(\theta_{inc})^4$ in the Fourier domain of this configuration, as was mentioned before. The SSNR_V^{inc} plot for this configuration even decreases with the angle of incidence of the obliquely incident plane waves, also for the theoretically approximated value according to Eq. (24). The reason for this is that the magnitude of the axial peaks is proportional to $1 + \cos(\theta_{inc})$ (see Appendix), so that their contribution to SSNR_V decreases quickly with θ_{inc} .

The SSNR_V^{inc} plots allow to check how well the approximation of separated OTF copies in Fourier space holds. Our results show that at high angles of incidence the agreement with Eq. (24) is perfect, while at low angles deviations are observed. This is understandable, as then there is more overlap between the displaced OTF copies in Fourier space. We also notice that the deviation in SSNR volume from the theoretical approximation can be either an undershoot or

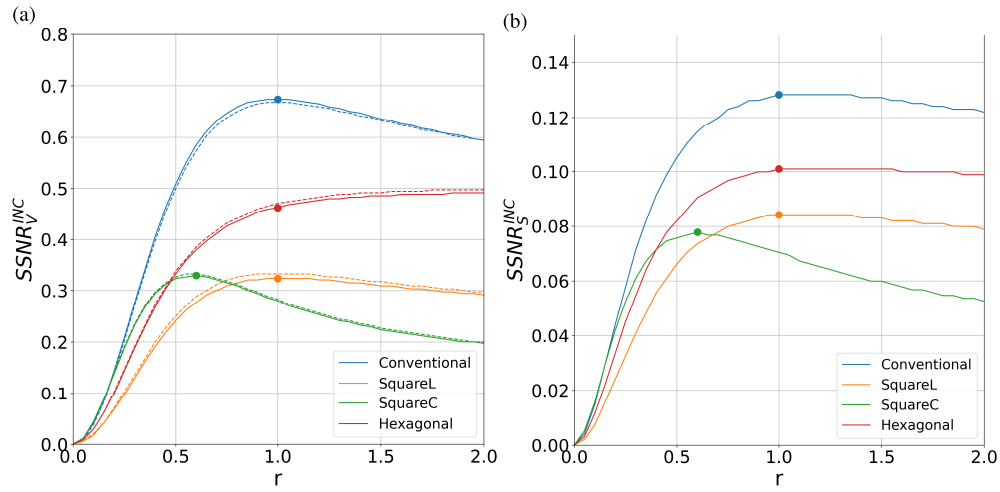


Fig. 5. Relative increase in SSNR volume $SSNR_V^{inc}$ (a) and SSNR entropy $SSNR_S^{inc}$ (b) for the 3D-SIM configurations of interest as a function of the ratio r between the amplitudes of the obliquely incident plane waves and the normally incident plane wave. Dashed lines in (a) show the theoretically approximated value of $SSNR_V^{inc}$ according to Eq. (24) and the solid lines represent the numerically calculated values by summing over the voxels in Fourier space. The values of $SSNR_V^{inc}$ and $SSNR_S^{inc}$ that correspond to the optimally chosen parameters are indicated with circles.

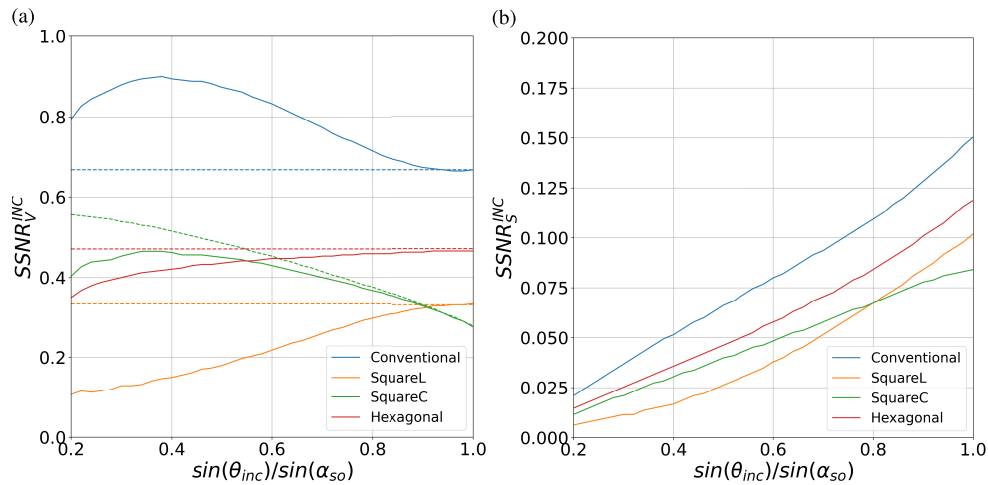


Fig. 6. Relative increase in (a) SSNR volume $SSNR_V^{inc}$ and (b) SSNR entropy $SSNR_S^{inc}$ for the 3D-SIM configurations of interest as a function of the normalized position of the obliquely incident plane wave peak in the BFP of the objective lens. The dashed lines corresponds to the theoretically approximated value of $SSNR_V^{inc}$ according to Eq. (24) and the solid lines represent the numerically calculated values by summing over the voxels in Fourier space.

an overshoot. This depends on how the polarization of the plane waves influences the relative phase of overlapping Fourier orders, and is thus subject to the design of the spatially periodic illumination patterns. The reduction of SSNR volume for square lattice SIM with circularly polarized obliquely incident plane waves originates from overlaps of laterally shifted OTF copies, whereas the reduction for square lattice SIM with linearly polarized obliquely incident plane waves originates from overlaps of axially shifted OTF copies. This is also apparent from the curves in Fig. 4, which show that the circular polarization case performs worse in the lateral direction but better in the axial direction compared to the linear polarization case. The good SSNR performance for conventional SIM originates mostly from the overlap of the axially shifted first order OTF copies, which have zero phase difference. We will discuss the effects of the overlap of axially shifted OTF copies in more details in the following section, emphasizing that the increase or decrease of the SSNR transfer function in the above-mentioned configurations depends on the illumination parameters.

Another aspect where the polarization and relative phase of the normally incident plane wave with respect to the obliquely incident ones has impact is the (lack of) symmetry in the final SSNR. Figure 7 shows the SSNR transfer function of square lattice SIM with circularly polarized waves along the q_x and q_y axes in the plane $q_z \approx 0.21$ ACF. We have chosen the illumination plane waves in such a way that the obliquely incident plane waves interfere destructively at the coordinate center $\vec{r} = \vec{0}$ (see Appendix). If the x and y -projections of the electric field of the normally incident wave are not equal at this point, a difference between the SSNR curves along the different axes is observed, i.e. an anisotropy in the SSNR arises. If they are the same, the SSNR curves become identical (phase shift = $\pi/4$ case). A phase shift of $\pi/2$ switches the roles of the axes, and a phase shift of π returns the electric field to the xz -plane, and the SSNR in this case equals to the one for zero phase shift. The dependence of the SSNR on this phase choice is small, however, noticeable only in the lower SSNR regions.

This effect is a consequence of the reconstruction procedure for 3D-SIM, which is, strictly speaking, not 3D, as only two-dimensional displacements of the illumination pattern are used. The reconstruction of spatial frequencies with high q_z is made possible because the illumination pattern is kept fixed w.r.t. the image plane of the microscope but not w.r.t. the sample [17]. As a result, the axially displaced copies of the OTF sharing the same lateral coordinates of the center, are seen by the reconstruction procedure as one effective OTF (defined by Eq. (16)). In conventional 3D-SIM this happens for the 1st order illumination pattern Fourier components. These copies are fully separated in the axial direction when the illumination plane wave angle of incidence is equal to the semi-opening angle of the lens, but overlap to some degree in the realistic case when the incidence angle is somewhat smaller. The signal transfer of those spatial frequencies that belong to both axially displaced OTF copies can then be amplified or diminished, depending on the illumination coefficients a_{mp} (see Appendix). This effect is compensated to a large extent by the fact that the affected spatial frequencies also receive signal via the central 0th order OTF copy, and the zeroth order illumination Fourier peak is generally much higher than the others. It does explain, however, the increase in SSNR volume of conventional 3D-SIM at small angles of incidence of the obliquely incident waves, as seen in Fig 6. The first order illumination pattern Fourier coefficients $a_{101}, a_{10-1}, a_{-101}, a_{-10-1}$ are all the same for this configuration (see Appendix), as all three incident waves interfere constructively in the focal plane, and an amplified SSNR transfer function is observed in all lateral directions of spatial frequency space. If instead the relative phases of the plane waves are chosen sub-optimally, the axially displaced OTF copies interfere destructively in the sum over displaced OTF copies that appears in the SSNR expression. In such cases, we see a reduction of signal transfer and hence decrease in SSNR volume. This is also the reason for the reduction in SSNR volume for square lattice SIM with linearly polarized waves in Fig. 6). We conclude that it matters for SIM to have the highest contrast in the focal plane: the woodpile structure of conventional SIM or its two-dimensional analogue for square

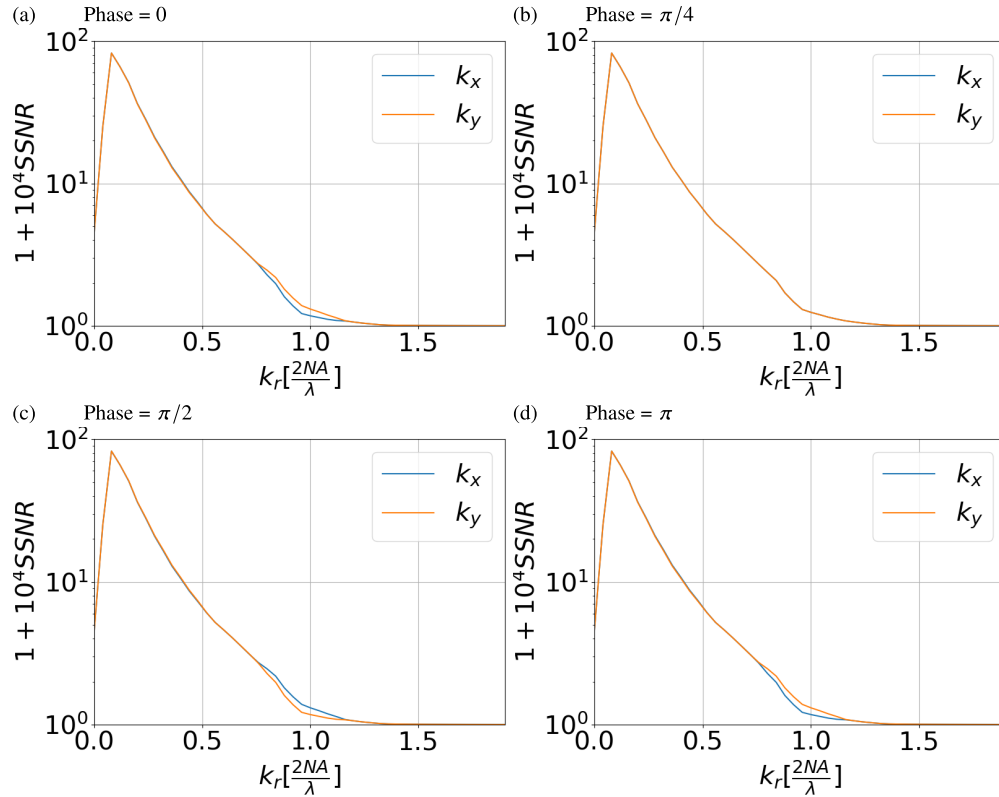


Fig. 7. Dependence of the SSNR along k_x and k_y directions on the relative phase of the normally incident waves in the configuration with five incoming circularly polarized waves (SquareC). a) Phase = 0. b) Phase = $\pi/4$. c) Phase = $\pi/2$. d) Phase = π

lattice SIM with linearly polarized waves must have its brightest spots in the focal plane for optimal signal transfer and hence SSNR.

To further illustrate this point we computed the ratios of $SSNR_V$ and $SSNR_S$ for constructive (designated with '+') and destructive (designated with '-') interference cases for conventional SIM. At $\sin \theta_{inc}/\sin \alpha_{so} = 0.9$, that corresponds to the situation of highest practical relevance, $SSNR_V^{inc+}/SSNR_V^{inc-} \approx 1.04$ and $SSNR_S^{inc+}/SSNR_S^{inc-} \approx 1.01$. This difference is very small. However, if $\sin \theta_{inc}/\sin \alpha_{so} = 0.5$, then $SSNR_V^{inc+}/SSNR_V^{inc-} \approx 2.4$ and $SSNR_S^{inc+}/SSNR_S^{inc-} \approx 1.5$. This means that if, for some reason, a high angle of incidence of obliquely incident waves is not achievable, the alignment of the woodpile pattern with the image plane by correctly setting the relative phases of the plane waves becomes crucial.

The anisotropy in square lattice 3D-SIM is due to the signal amplification in one direction and reduction in another. Any configuration with a circularly polarized normally incident wave will suffer from directional anisotropy. In the case of square lattice 3D-SIM, these can be eliminated by a correct choice of phase.

Hexagonal lattice 3D-SIM is theoretically even more complicated. It is not possible to select the initial phase of the incoming plane wave to completely get rid of anisotropies, because the polarization direction cannot be equally aligned with all three hexagonal diagonals. Moreover, if one of the incoming oblique plane waves has a phase offset, it can lead to yet another kind of anisotropy, caused by a change of magnitude of the illumination peaks in the Fourier domain.

The magnitude of this anisotropy effect turns out to be rather small, the influence of anisotropy for hexagonal lattice 3D-SIM in our simulations is barely noticeable. We also checked if a circularly polarized central wave can be used instead of linear polarization at the angle of 45° in the square lattice 3D-SIM configuration, and found that for high illumination angles of incidence the SSNR transfer function anisotropy is negligible.

So far, all simulations were performed for the case of an ideal emission PSF. However, in real experiments aberrations are always present to some extent. We have compared changes between the SIM configurations in the SSNR metrics as a function of aberration strength for the three most common aberrations, namely primary (Zernike) spherical aberration, coma and astigmatism. It appears there are hardly differences between the SIM configurations in how SSNR volume decreases with aberration strength, due to the high degree of separation of the OTF copies in Fourier space. In fact, the curves nearly coincide with the curve for the widefield case. In contrast, SSNR entropy does show different aberration response between SIM configurations. Figure 8 shows the decrease in SSNR entropy with aberration strength for the three primary aberration modes. First, it appears that all SIM modes outperform the widefield case. This may be due to the spatial frequencies near the centers of the OTF copies in Fourier space that are relatively unaffected by aberrations, leading to a distribution of SSNR across spatial frequencies that is more robust to perturbation by aberrations. Second, conventional and hexagonal lattice SIM have slightly better aberration sensitivity than square lattice SIM. The intuition behind this is that aberrations primarily affect the transfer of intermediate spatial frequencies, and with the more isotropic SIM configurations there is more overlap of OTF orders to suppress this. The third point of relevance is that the resilience towards rotationally symmetric aberrations like spherical aberration is higher than towards asymmetric aberrations like astigmatism and coma.

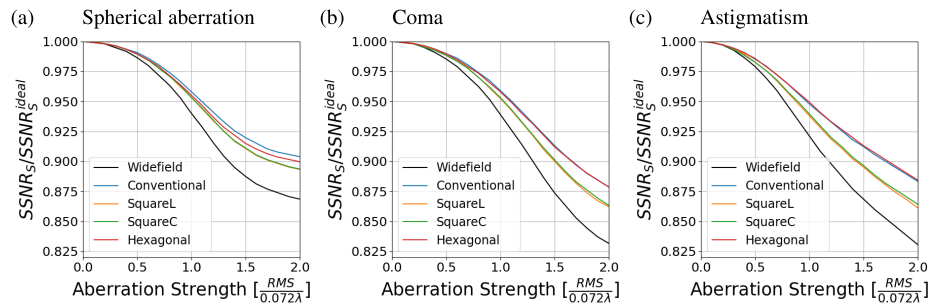


Fig. 8. SSNR entropy of the different SIM configurations as a function of aberration strength for the three primary Zernike aberrations, spherical aberration (a), coma (b), and astigmatism (c). The aberration strength (root means square Zernike coefficient) is measured in units of Maréchal's diffraction limit ($\lambda/(8\sqrt{3}) = 0.072\lambda$).

4. Conclusion

In summary, we considered different 3D-SIM illumination configurations and calculated the spectral signal-to-noise ratio (SSNR) in the shot-noise dominated regime to evaluate their potential performance. In particular, we compared conventional 3D-SIM based on a woodpile shaped illumination pattern that is translated and rotated for making a super-resolution reconstruction possible to lattice 3D-SIM based on illumination patterns that only need translations. We addressed lattice 3D-SIM configurations that use symmetric illumination patterns found in the literature: square and hexagonal. It was shown that conventional 3D-SIM has superior SSNR performance compared to all considered lattice 3D-SIM configurations. This assessment is based on the SSNR transfer function, which separates out any sample effects, the illumination

dose and light detection efficiency on the SSNR. This means that the comparison assumes constant total illumination dose, and that a better SSNR is predicted for conventional 3D-SIM with the same amount of phototoxicity and photobleaching. In other words, to achieve the image quality of conventional SIM with lattice SIM, more photodamage must be delivered to the sample. Even though lattice 3D-SIM does not yield as good SSNR as conventional woodpile illumination 3D-SIM, it does offer some advantages in terms of experimental complexity and potential acquisition speed. For lattice 3D-SIM there is no need to rotate the polarization of the central illumination beam, it can remain fixed. Furthermore, rotation of the illumination pattern, either by rotating a dove prism or the diffraction grating that produces the required set of illumination beams, or by using complex optical devices such as Spatial Light Modulators (SLMs), is not needed in the experimental setup. A 2D translation of a diffraction grating for generating the different illumination beams by piezo elements, and static means to change the polarization of the illumination beams are sufficient for lattice 3D-SIM.

We introduced two global metrics with clear physical meaning, SSNR volume and SSNR entropy, allowing a quick comparison of the global behavior of SSNR in the whole spatial frequency domain. These metrics can be used to compare the different illumination configurations, to search for optimal experimental parameters, or to test theoretically made assumptions.

We demonstrated that the polarization of the incoming plane waves is relevant for the overall imaging performance in 3D-SIM. In particular, we considered a square lattice 3D-SIM configuration where the five contributing plane waves have the same circular polarization. This may be advantageous from an experimental point of view and because more Fourier components participate in the Fourier transform of the illumination pattern compared to square lattice 3D-SIM based on linearly polarized incident plane waves, which could lead to a more uniform improvement of SSNR across spatial frequency space. It turned out, however, that this configuration has poor SSNR performance at high spatial frequencies. Another drawback that was revealed is that the choice of phase of the normally incident wave matters if it is circularly polarized, as it leads, in general, to anisotropy of the SSNR transfer function. This effect is a direct consequence of the entire underlying theory of projective 3D-SIM [17]. It was shown that for small angles of incidence, the choice of relative phases of all participating plane waves becomes important for configurations with linearly polarized waves as well. In particular, both pattern shape and position w.r.t. the focal plane matters in for 3D-SIM.

We investigated the impact of a deviation from the ideal scalar OTF due to aberrations, by simulating the decay of the SSNR global metrics with aberration strength. It appears that conventional SIM and lattice with hexagonal symmetry outperform square lattice SIM, and that all SIM configurations outperform the widefield case. A different deviation from the ideal OTF we did not consider is related to the assumption that a high-NA scalar PSF model is applicable. Polarization effects in the emission light path are hence ignored in the analysis. This includes polarization-dependent transmission effects at interfaces between media with potential refractive index mismatch (sample - cover glass and cover glass - immersion fluid). However, the overall conclusions of this work can be expected to be insensitive to the precise shape of the OTF, as its highly peaked nature in 3D incoherent imaging systems plays a crucial role here.

In this work, we only considered 3D-SIM configurations that obey the orthogonality condition of Eq. (9) for the illumination patterns, which provide a sufficient condition to extract the image Fourier orders from the raw images. The closed form Eqs. (13) and (14) are only valid under this constraint. It is also a sufficient, but not necessary, condition for having a total light exposure that is uniform everywhere in the field of view. We have not investigated how deviations from this assumption affect SSNR, although it seems likely from the theory of Ref. [27] that a violation of the orthogonality condition Eq. (9) will lead to a growth of the noise power. This may be of relevance for (pseudo)-random illumination microscopy [36].

An illumination pattern generated with three incoming oblique plane waves has been considered to generate hexagonal interference patterns for 2D-SIM [37]. A disadvantage of this triangular interference is that plane waves, propagating at 120° angle with respect to each other, do not give as dense an interference pattern as those resulting from diametrically opposite plane waves. This reduces the achievable lateral resolution gain to $\sqrt{3}$ times the diffraction limit, as was also noticed in Ref. [37]. Moreover, the extension of this configuration to 3D-SIM by adding a normally incident plane wave lacks axial symmetry in the illumination pattern Fourier transform and hence SSNR transfer function (it is symmetric under the inversion but not reflection). Our assessment was that the triangular configuration is suboptimal for 3D-SIM and we did not analyze it further in this manuscript.

An extension of the current work is to consider families of configurations that belong to the same symmetry groups but show more complex axial behavior. For example, a lattice 3D-SIM configuration with square symmetry but eight obliquely incident plane waves split into two groups of four waves can be considered. Each group of four waves forms a square but have a different angle of incidence on the sample. Such a configuration could improve lateral SSNR isotropy. It would, however, be experimentally difficult to realize and would require a larger number of raw images to obtain a full super-resolution reconstruction. It is straightforward to extend the analysis of this work to the cases of SIM with enhanced axial resolution and beyond epi-illumination. Despite the considerable experimental complexity of such setups, systematic attempts in this direction are made by different groups [38–40]. In this case, compromise between axial and lateral SSNR may be shifted towards the former and the effect of a mutual phases of incoming plane waves may play a greater role.

Another extension of interest for the current analysis is to non-linear SIM [13], as under certain assumptions lattice 2D-SIM configurations can result in better SNR in the non-linear regime [31], as opposed to the linear regime, where we showed that conventional 3D-SIM has better SSNR than lattice 3D-SIM. Possible realizations of non-linear SIM include SIM with saturation of fluorescent labels [13], SIM with reversibly photoswitchable fluorescent labels [31] and SIM with stimulated emission depletion [14]. The illumination-dependent response is different in these cases, and hence optimal illumination parameters or, possibly, configurations with optimal SSNR metrics could be different. The combination of SIM and light-sheet microscopy [41–43] is a promising investigation direction as well. We can envision better axial SSNR, as optical sectioning is now achieved physically rather than computationally, especially when normalized for the total absorbed illumination dosage. It could also be fruitful to compare the SSNR performance of SIM against other super-resolution methods based on non-uniform illumination, such as ISM or RCM [6,8,44], and (pseudo-)random illumination microscopy [36]. Such a study would provide an inroad to the interesting question which of the super-resolution flavour in the family that gives up to twofold improvement over the diffraction limit is fundamentally better.

Finally, the introduced SSNR metrics could be used for a quantitative analysis of the SIM reconstruction procedure itself, looking, for example, at effects of additional filtering, such as notch filtering, or at spatial domain reconstructions [25,45].

Appendix

The illumination electric field for the four considered SIM configurations is:

- Conventional SIM:

$$\begin{aligned}\vec{E} = & r(0, 1, 0) \exp(i(k \sin(\theta)x + k \cos(\theta)z)) \\ & + r(0, 1, 0) \exp(i(-k \sin(\theta)x + k \cos(\theta)z)) \\ & + (0, 1, 0) \exp(ikz)\end{aligned}\quad (25)$$

- Square lattice SIM with linearly polarized waves:

$$\begin{aligned}\vec{E} = & r(0, 1, 0) \exp(i(k \sin(\theta)x + k \cos(\theta)z)) \\ & + r(0, -1, 0) \exp(-i(k \sin(\theta)x + k \cos(\theta)z)) \\ & + r(1, 0, 0) \exp(i(k \sin(\theta)y + k \cos(\theta)z)) \\ & + r(-1, 0, 0) \exp(-i(k \sin(\theta)y + k \cos(\theta)z)) \\ & + (1, -1, 0) \exp(ikz)\end{aligned}\quad (26)$$

Table 1. Fourier structure of the illumination configurations. The positions of the peaks in Fourier space are given by numerical factors m_x, m_y, m_z of the corresponding 3D Bravais lattice vectors $\vec{k} = m_x k \sin \theta \hat{x} + m_y k \sin \theta \hat{y} + m_z k (1 - \cos \theta) \hat{z}$. In the computation of the SSNR all Fourier component magnitudes are normalized by the (0, 0, 0) component. a) State-of-the-art 3D-SIM based on small pitch woodpile illumination pattern ("Conventional"). b) Square lattice 3D-SIM with linearly polarized plane waves ("SquareL"). c) Square lattice 3D-SIM with circularly polarized plane waves ("SquareC"). d) Hexagonal lattice SIM with linearly polarized plane waves ("Hexagonal").

(a) Conventional		(b) SquareL			
Position	Magnitude	Position	Magnitude	Position	Magnitude
(0, 0, 0)	$1 + 2r^2$	(0, 0, 0)	$2 + 4r^2$	$\pm(0, 1, 1)$	$-r$
$(\pm 2, 0, 0)$	r^2	$(\pm 2, 0, 0)$	$-r^2$	$\pm(0, 1, -1)$	r
$(\pm 1, 0, \pm 1)$	r	(0, $\pm 2, 0$)	$-r^2$	$\pm(1, 0, 1)$	r
				$\pm(1, 0, -1)$	$-r$

(c) SquareC			
Position	Magnitude	Position	Magnitude
(0, 0, 0)	$2 + 8r^2$	$\pm(1, 0, 1)$	$-(1 + \cos(\theta)r)$
$(\pm 2, 0, 0)$	$-2r^2 \cos(\theta)^2$	$\pm(-1, 0, 1)$	$(1 + \cos(\theta)r)$
(0, $\pm 2, 0$)	$-2r^2 \cos(\theta)^2$	(0, 1, ± 1)	$-i(1 + \cos(\theta)r)$
$(\pm 1, \pm 1, 0)$	$-2r^2 \sin(\theta)^2$	(0, -1, ± 1)	$i(1 + \cos(\theta)r)$

(d) Hexagonal			
Position	Magnitude	Position	Magnitude
(0, 0, 0)	$2 + 6r^2$		
$(\pm 2, 0, 0)$	$-r^2$	$(1/2, \sqrt{3}/2, \pm 1)$	$((\mp\sqrt{3} - i)/2)r$
$(\pm 1, \pm\sqrt{3}, 0)$	$-r^2$	$(-1/2, \sqrt{3}/2, \pm 1)$	$((\mp\sqrt{3} + i)/2)r$
(0, $\pm\sqrt{3}, 0$)	$-r^2$	$(1/2, -\sqrt{3}/2, \pm 1)$	$((\pm\sqrt{3} - i)/2)r$
$(\pm 3/2, \pm\sqrt{3}/2, 0)$	$-r^2$	$(-1/2, -\sqrt{3}/2, \pm 1)$	$((\pm\sqrt{3} + i)/2)r$
$(\pm 1, 0, 0)$	r^2	(1, 0, ± 1)	$-ir$
$(\pm 1/2, \pm\sqrt{3}/2, 0)$	r^2	(-1, 0, ± 1)	ir

- Square lattice SIM with circularly polarized waves:

$$\begin{aligned} \vec{E} = & r(\cos(\theta), i, -\sin(\theta)) \exp(i(k \sin(\theta)x + k \cos(\theta)z)) \\ & + r(-\cos(\theta), -i, -\sin(\theta)) \exp(i(-k \sin(\theta)x + k \cos(\theta)z)) \\ & + r(-i, \cos(\theta), -\sin(\theta)) \exp(i(k \sin(\theta)y + k \cos(\theta)z)) \\ & + r(i, -\cos(\theta), -\sin(\theta)) \exp(i(-k \sin(\theta)y + k \cos(\theta)z)) \\ & + (1, i, 0) \exp(ikz) \end{aligned} \quad (27)$$

- Hexagonal lattice SIM:

$$\begin{aligned} \vec{E} = & \sum_{j=0}^5 r \left(-\sin\left(\frac{2\pi j}{3}\right), \cos\left(\frac{2\pi j}{3}\right), 0 \right) \times \\ & \exp\left(ik \left(\sin\theta \cos\left(\frac{2\pi j}{3}\right) x + \sin\theta \sin\left(\frac{2\pi j}{3}\right) y + \cos\theta z \right) \right) \\ & + (1, i, 0) \exp(ikz) \end{aligned} \quad (28)$$

In all cases the amplitude parameter r is defined as the ratio of the s amplitude of the obliquely incident plane wave component and the x or y component of the normally incident plane wave component. In the subsequent computation of the SSNR the spatially averaged intensity is normalized to unity. The resulting illumination intensity has peaks in Fourier space at positions $\vec{k} = m_x k \sin\theta \hat{x} + m_y k \sin\theta \hat{y} + m_z k (1 - \cos\theta) \hat{z}$, with numerical prefactors m_x, m_y, m_z and with magnitudes as provided in Table 1. We mention that this parametrization of the Fourier peaks does not correspond to an expansion in basis vectors of the Bravais lattice.

The illumination pattern peaks in Fourier space for the four considered SIM configurations are further illustrated in Fig. 9.

Funding. HORIZON EUROPE European Research Council (101055013).

Disclosures. The authors declare no conflicts of interest.

Data availability. The software is available at [46].

References

1. R. Heintzmann and C. Cremer, "Laterally modulated excitation microscopy: Improvement of resolution by using a diffraction grating," *Proc. SPIE* **3568**, 185–196 (1999).
2. M. G. L. Gustafsson, "Surpassing the lateral resolution limit by a factor of two using structured illumination microscopy," *J. Microsc.* **198**(2), 82–87 (2000).
3. K. Samanta and J. Joseph, "An overview of structured illumination microscopy: Recent advances and perspectives," *J. Opt.* **23**(12), 123002 (2021).
4. S. J. Wright and D. J. Wright, "Introduction to confocal microscopy," in *Methods in Cell Biology*, vol. 70, (Elsevier Science, 2002), pp. 1–85.
5. M. A. A. Neil, R. Juškaitis, and T. Wilson, "Real time 3D fluorescence microscopy by two beam interference illumination," *Opt. Commun.* **153**(1-3), 1–4 (1998).
6. C. B. Müller and J. Enderlein, "Image scanning microscopy," *Phys. Rev. Lett.* **104**(19), 198101 (2010).
7. C. J. R. Sheppard, S. B. Mehta, and R. Heintzmann, "Superresolution by image scanning microscopy using pixel reassignment," *Opt. Lett.* **38**(15), 2889–2892 (2013).
8. G. M. R. D. Luca, R. M. P. Breedijk, R. A. J. Brandt, *et al.*, "Re-scan confocal microscopy: scanning twice for better resolution," *Biomed. Opt. Express* **4**(11), 2644–2656 (2013).
9. M. G. L. Gustafsson, D. A. Agard, and J. W. Sedat, "I5M: 3D widefield light microscopy with better than 100 nm axial resolution," *J. Microsc.* **195**(1), 10–16 (1999).
10. K. Bahlmann, S. Jakobs, and S. W. Hell, "4Pi-confocal microscopy of live cells," *Ultramicroscopy* **87**(3), 155–164 (2001).
11. A. G. York, S. H. Parekh, D. D. Nogare, *et al.*, "Resolution doubling in live, multicellular organisms via multifocal structured illumination microscopy," *Nat. Methods* **9**(7), 749–754 (2012).
12. N. Chakrova, R. Heintzmann, B. Rieger, *et al.*, "Studying different illumination patterns for resolution improvement in fluorescence microscopy," *Opt. Express* **23**(24), 31367–31383 (2015).

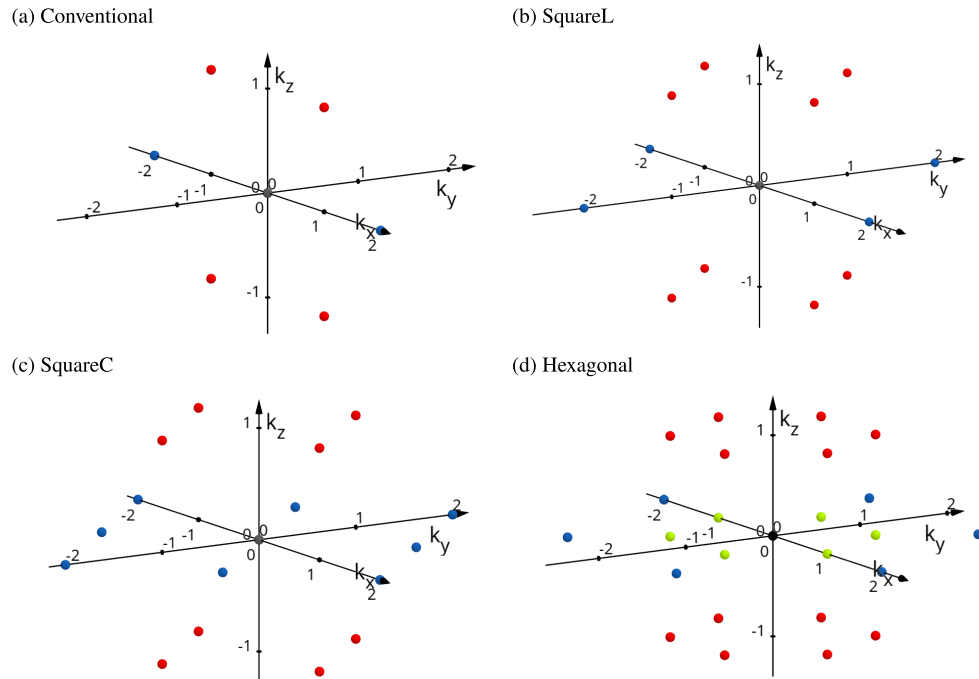


Fig. 9. Schematic illustration of Fourier transform of the intensity pattern of the considered configurations. Units: $[k_x] = [k_y] = k \sin \theta_{inc}$, $[k_z] = k(\cos \theta_{inc} - 1)$. a) State-of-the-art 3D-SIM based on small pitch woodpile illumination pattern ("Conventional"). b) Square lattice 3D-SIM with linearly polarized plane waves ("SquareL"). c) Square lattice 3D-SIM with circularly polarized plane waves ("SquareC"). d) Hexagonal lattice SIM with linearly polarized plane waves ("Hexagonal"). Blue and green indicate components in the plane $k_z = 0$ (different colours used for the sake of visibility), red indicates components out of the plane $k_z = 0$.

13. M. G. L. Gustafsson, "Nonlinear structured-illumination microscopy: Wide-field fluorescence imaging with theoretically unlimited resolution," *Proc. Natl. Acad. Sci.* **102**(37), 13081–13086 (2005).
14. Y. Xue and P. T. C. So, "Three-dimensional super-resolution high-throughput imaging by structured illumination STED microscopy," *Opt. Express* **26**(16), 20920–20928 (2018).
15. M. Neil, R. Juškaitis, and T. Wilson, "Method of obtaining optical sectioning by using structured light in a conventional microscope," *Opt. Lett.* **22**(24), 1905–1907 (1997).
16. T. Breuninger, K. Greger, and E. H. K. Stelzer, "Lateral modulation boosts image quality in single plane illumination fluorescence microscopy," *Opt. Lett.* **32**(13), 1938–1940 (2007).
17. M. G. L. Gustafsson, L. Shao, P. M. Carlton, *et al.*, "Three-dimensional resolution doubling in wide-field fluorescence microscopy by structured illumination," *Biophys. J.* **94**(12), 4957–4970 (2008).
18. J. D. Manton, F. Ströhl, R. Fiolka, *et al.*, "Concepts for structured illumination microscopy with extended axial resolution through mirrored illumination," *Biomed. Opt. Express* **11**(4), 2098–2108 (2020).
19. X. Chen, S. Zhong, Y. Hou, *et al.*, "Superresolution structured illumination microscopy reconstruction algorithms: a review," *Light:Sci. Appl.* **12**(1), 172 (2023).
20. T. A. Hinsdale, S. Stallinga, and B. Rieger, "High-speed multicolor structured illumination microscopy using a hexagonal single mode fiber array," *Biomed. Opt. Express* **12**(2), 1181–1194 (2021).
21. M. Schropp and R. Uhl, "Two-dimensional structured illumination microscopy," *J. Microsc.* **256**(1), 23–36 (2014).
22. J. Siebenmorgen, Y. Novikau, R. Wolleschensky, *et al.*, "Introducing lattice SIM for ZEISS Elyra 7: Structured illumination microscopy with a 3D lattice for live cell imaging," Technology note, Carl Zeiss Microscopy GmbH (2018).
23. J. Zheng, "Large-field lattice structured illumination microscopy," *Opt. Express* **30**(15), 27951 (2022).
24. Q. Liu, D. Zhou, J. Zhang, *et al.*, "DMD-based compact SIM system with hexagonal-lattice-structured illumination," *Appl. Opt.* **62**(20), 5409–5415 (2023).

25. T. Zhao, Z. Wang, M. Shu, *et al.*, “Instant square lattice structured illumination microscopy: an optimal strategy towards photon-saving and real-time super-resolution observation,” *arXiv* (2024).
26. L. Z. Cai, X. L. Yang, and Y. R. Wang, “All fourteen Bravais lattices can be formed by interference of four noncoplanar beams,” *Opt. Lett.* **27**(11), 900–902 (2002).
27. C. S. Smith, J. A. Slotman, L. Schermelleh, *et al.*, “Structured illumination microscopy with noise-controlled image reconstructions,” *Nat. Methods* **18**(7), 821–828 (2021).
28. G. Ball, J. Demmerle, R. Kaufmann, *et al.*, “SIMcheck: a toolbox for successful super-resolution structured illumination microscopy,” *Sci. Rep.* **5**(1), 15915 (2015).
29. S. Culley, D. Albrecht, C. Jacobs, *et al.*, “Quantitative mapping and minimization of super-resolution optical imaging artifacts,” *Nat. Methods* **15**(4), 263–266 (2018).
30. D. Li, L. Shao, B.-C. Chen, *et al.*, “Extended-resolution structured illumination imaging of endocytic and cytoskeletal dynamics,” *Science* **349**(6251), aab3500 (2015).
31. E. A. Ingerman, R. A. London, R. Heintzmann, *et al.*, “Signal, noise and resolution in linear and nonlinear structured-illumination microscopy,” *J. Microsc.* **273**(1), 3–25 (2019).
32. M. Gu, *Advanced Optical Imaging Theory, vol. 75 of Springer Series in Optical Sciences* (Springer, Berlin, Heidelberg, 2000).
33. S. Stallinga and B. Rieger, “Accuracy of the Gaussian point spread function model in 2D localization microscopy,” *Opt. Express* **18**(24), 24461–24476 (2010).
34. R. P. J. Nieuwenhuizen, K. A. Lidke, M. Bates, *et al.*, “Measuring image resolution in optical nanoscopy,” *Nat. Methods* **10**(6), 557–562 (2013).
35. B. Rieger, I. Droste, F. Gerritsma, *et al.*, “Single image fourier ring correlation,” *Opt. Express* **32**(12), 21767–21782 (2024).
36. E. Mudry, K. Belkebir, J. Girard, *et al.*, “Structured illumination microscopy using unknown speckle patterns,” *Nat. Photonics* **6**(5), 312–315 (2012).
37. C. Ji, Y. Zhu, E. He, *et al.*, “Full field-of-view hexagonal lattice structured illumination microscopy based on the phase shift of electro-optic modulators,” *Opt. Express* **32**(2), 1635–1649 (2024).
38. X. Li, Y. Wu, Y. Su, *et al.*, “Three-dimensional structured illumination microscopy with enhanced axial resolution,” *Nat. Biotechnol.* **41**(9), 1307–1319 (2023).
39. Z. Ouyang, Q. Wang, X. Li, *et al.*, “Elucidating subcellular architecture and dynamics at isotropic 100-nm resolution with 4Pi-SIM,” *Nat. Methods* **22**(2), 335–347 (2025).
40. J. Joseph, K. P. Faiz, M. Lahrberg, *et al.*, “Improving the space-bandwidth product of structured illumination microscopy using a transillumination configuration,” *J. Phys. D: Appl. Phys.* **53**(4), 044006 (2020).
41. R. Li, D. Wu, X. Zhou, *et al.*, “Selective plane illumination microscopy with structured illumination based on spatial light modulators,” in *Proceedings of SPIE – The International Society for Optical Engineering*, (2014) Conference Paper.
42. K. Temma, R. Oketani, T. Kubo, *et al.*, “Selective-plane-activation structured illumination microscopy,” *Nat. Methods* **21**(5), 889–896 (2024).
43. B. Chen, B. J. Chang, P. Roudot, *et al.*, “Resolution doubling in light-sheet microscopy via oblique plane structured illumination,” *Nat. Methods* **19**(11), 1419–1426 (2022).
44. C. J. R. Sheppard, “Super-resolution in confocal imaging,” *Optik* **80**, 53–54 (1988).
45. D. Dan, Z. Wang, X. Zhou, *et al.*, “Rapid image reconstruction of structured illumination microscopy directly in the spatial domain,” *IEEE Photonics J.* **13**(1), 1–11 (2021).
46. V. Brudanin, “Software for the calculations of noise in SIM,” 1.0 Github (2024) <https://github.com/valbrud/SIM>